

Full paper

In situ tem investigation on ultrafast reversible lithiation and delithiation cycling of Sn@C yolk-shell nanoparticles as anodes for lithium ion batteries



Ke Cao^{a,1}, Peifeng Li^{b,*,1}, Yizhi Zhang^b, Tianwu Chen^c, Xu Wang^d, Sulin Zhang^c, Jiabin Liu^{a,*}, Hongtao Wang^{b,*}

^a Department of Materials Science and Engineering, State Key Laboratory of Silicon Materials, Zhejiang University, Hangzhou 310027, Zhejiang, China

^b Institute of Applied Mechanics, Zhejiang University, Hangzhou 310027, Zhejiang, China

^c Engineering Science and Mechanics, Pennsylvania State University, University Park, PA 16801, United States

^d Department of Physics, Zhejiang University, Hangzhou 310027, Zhejiang, China

ARTICLE INFO

Keywords:

Sn@C yolk-shell nanoparticles
In situ transmission electron microscope
 Ultrafast
 Reversible lithiation and delithiation
 Front-track finite element analysis
 Constraint effects

ABSTRACT

Surface coating has become an effective method to stabilize solid-electrolyte interphase (SEI), extend the cycle life, and improve rate performance of anode materials for lithium ion batteries (LIBs). However, owing to the incompatible volumetric changes between the core and the shell, core-shell structures with fully filled active materials are prone to fracture upon electrochemical cycling, leading to fast capacity fading. Here, we synthesize partially filled Sn@C yolk-shell nanoparticles (NPs) by chemical vapor deposition (CVD) as anode materials for LIBs. Our *in situ* transmission electron microscope (TEM) studies demonstrate that the yolk-shell NPs can lithiate and delithiate hundreds of cycles with ultrafast (2 s per cycle) reversible cycling without rupture. Front-tracking finite element analysis of the coupled chemical reaction, diffusion, and stress generation upon lithiation reveals improved chemomechanical durability of the yolk-shell NPs, in comparison to naked SnNPs and fully filled Sn@C core-shell NPs. Our results provide rational guidance to the development and optimization of yolk-shell NPs as high-performance anode materials for LIBs.

1. Introduction

The rapidly growing demand for high-performance lithium ion batteries (LIBs) has driven relentless research work to design and synthesize new electrode materials with high energy density, high power, and long cycle life [1–4]. Graphite [5], the most commonly used anodes in commercial LIBs, has a relatively low energy density (375 mAh g⁻¹, ≈ 1000 mAh ml⁻¹) and thus falls behind the demand. Enormous effort has recently been devoted to high-capacity anode materials, including Si, Ge, Sn and oxide materials such as SnO₂ and FePO₄ [6–15]. However, these high-capacity anode materials undergo large volumetric swelling and are prone to rupture upon lithiation, which subsequently lead to unstable solid-electrolyte interface (SEI) growth, loss of contact between active materials, binders, and current collectors, and eventually fast capacity fading. In mitigating the chemomechanical degradation of these high-capacity electrode materials, many innovative strategies have been developed, including nanostructuring, compositing, porosity, and surface coating, etc., all of which have improved the electrochemical performance of the electrode materials to a great

extent.

Surface coating has been identified as a promising strategy to mitigate the chemomechanical degradation of the high-capacity electrodes. Surface coatings can function as a chemical barrier that separates active materials from liquid electrolyte, suppresses unwanted reactions between them, thereby stabilizing the SEI layer. Surface coatings can also function as a mechanical buffer layer that constrains the volumetric change during electrochemical cycling, thus preventing pulverization of the active core materials. Carbon, metal, and some polymeric coatings are electronically conductive, can enhance the redox reaction kinetics and improve the power performance. Huang et al. realized the ultrafast and full electrochemical lithiation of single Si nanowires (SiNWs) through carbon-coating [4]. Carbon coating has also been exploited to control lithiation-induced strain and charging rate in SnO₂ NWs [16]. Wang et al. observed that SiNPs coated with conductive polymer polypyrrole self-discharges due to the constraining effect of the coating [17]. Wang et al. studied the reversibility of SnNWs coated with carbon in lithiation and delithiation, and observed a two-step reversible crystalline-crystalline phase transformation [11].

* Corresponding authors.

E-mail addresses: peifengli@zju.edu.cn (P. Li), liujiabin@zju.edu.cn (J. Liu), htw@zju.edu.cn (H. Wang).

¹ These authors contributed equally to this work.

Ishihara et al. found that coating Si with carbon nanotube improves the cycle stability of the Si anode [18]. All these studies suggest that surface coating represents a powerful approach for improving capacity retention and cyclability of high-capacity electrodes.

Yolk-shell structure represents a special core-shell structure, which features movable cores and pre-reserved void space between the core and the shell. In general, the shell contributes negligibly to the overall capacity, but offers high conductivity and mechanical stability of the yolk-shell. During electrochemical cycling, the active yolk undergoes large volumetric changes without forming SEI, while the shell facing the electrolyte is covered with SEI but undergoes negligible volume

change. Owing to the pre-reserved void space, the active contents are fully confined in the closed shell throughout the cycling even though the yolk pulverizes. A larger yolk-to-void volumetric ratio is favored for the higher capacity. However, the pre-reserved void space must be sufficient; otherwise the volume expansion of the yolk would break the shell and subsequently the shell as well. Thus, the volumetric ratio of the active yolk and pre-reserved void space must be carefully designed and optimized in order to maximize the capacity but minimize the pulverization of the yolk-shell structure.

In this letter, partially-filled Sn@C yolk-shell NPs are designed and synthesized, and their phase transformation and microstructural

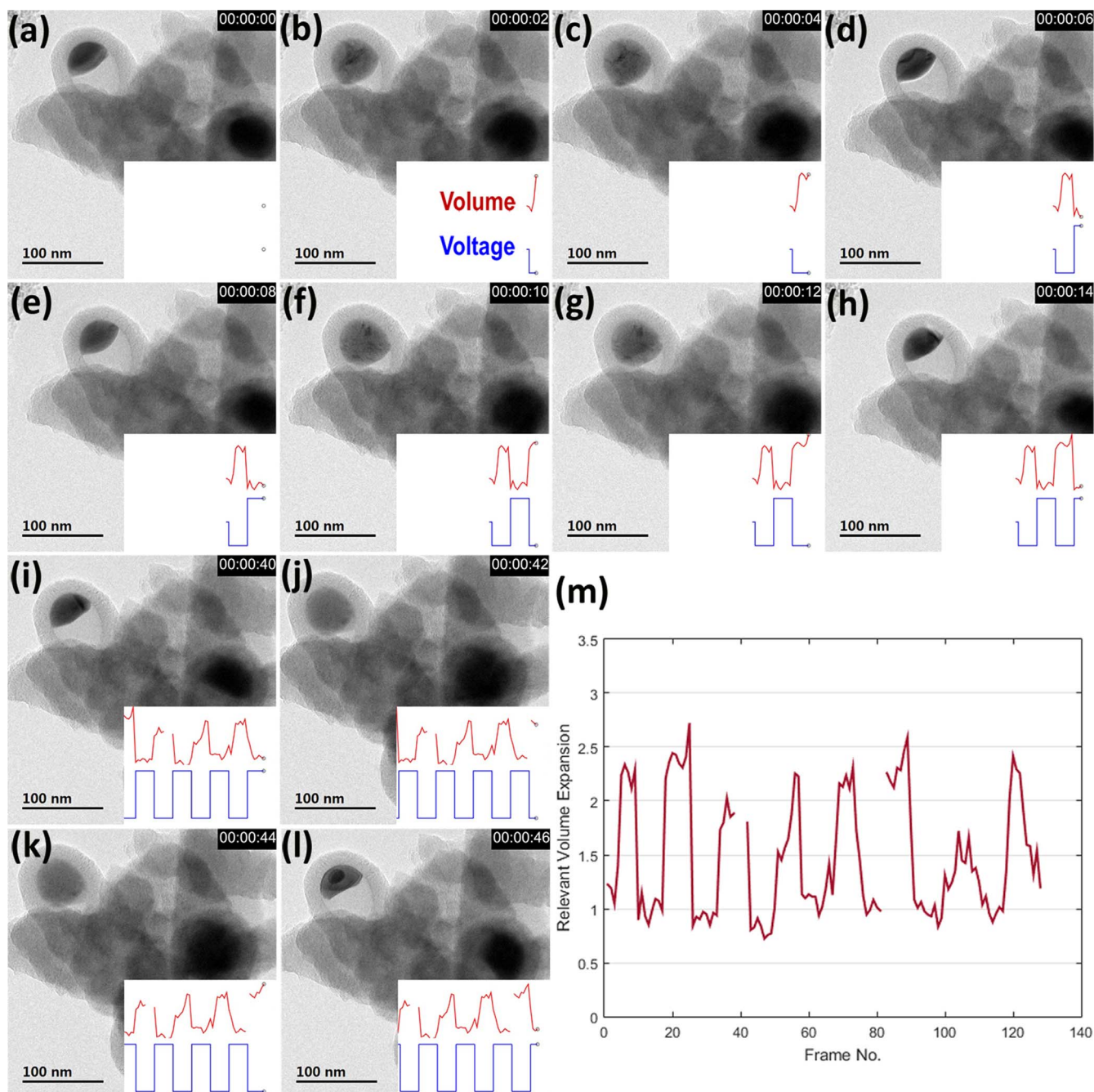


Fig. 1. *In situ* TEM reversible lithiation and delithiation of a Sn@C yolk-shell NPs attached on the C substrate with high energy capacity. (a-h) TEM images of the first two cycles (0–16 s, the image at 16 s is not shown here because it replies to the initial state like 0 s and 8 s) of reversible lithiation and delithiation process, the insert images show the volume changing of the target NP as the applied voltages in the reversible lithiation and delithiation process, the volume expansion even reaches to ~ 2.7 – 2.8 that can be calculated in (m) which shows the high energy capacity lithiation properties. (i-l) TEM images of the 6th cycle (40–48 s, the image at 48 s is also not shown here) of reversible lithiation and delithiation process. The volume curve Vs. voltage curve shows a perfect synchronization in the whole reversible lithiation and delithiation process. (m) The volume expansion in the whole reversible lithiation and delithiation simulated by Matlab. The lithiation and delithiation cycle time $t = 8$ s.

evolution upon electrochemical cycling are characterized by *in situ* TEM. Front tracking finite element analyses are invoked to simulate the chemical reaction, mass diffusion, lithiation-induced large deformation and stress generation. Our integrated experimental and modeling results evidence improved electrochemical performance of the Sn@C yolk-shell NPs in comparison to their naked and fully filled counterparts. Our studies shed light on material selection, fabrication, and optimization of novel yolk-shell structures as anode materials for LIBs.

2. Results and discussions

Fig. S1 shows the schematics of *in situ* TEM setting for characterizing the reversible lithiation and delithiation of partially filled Sn@C yolk-shell NPs. Reversible lithiation and delithiation cycling was preceded by applying a cyclical rectangular wave voltage [−4 V, 4 V]. The Sn@C yolk-shell NPs were lithiated in the first half loop with negative bias accompanied by volume expansion of the Sn core, while delithiated in the second half loop with positive bias accompanied with volume shrinkage of the Sn core.

2.1. High energy capacity lithiation performance

We first studied the capacity of the partially filled Sn@C yolk-shell NPs. Fig. 1a–j show a sequence of *in situ* TEM images of the reversible lithiation and delithiation of a Sn@C yolk-shell NP attached on a C substrate. The dynamics of lithiation and delithiation is also shown in Movie S1. Each lithiation-delithiation cycle time was tuned to be 8 s by controlling the signal function generator. Fig. 1a–h show the TEM images of the first two cycles (0–16 s). From the images we observed that the Sn yolk core underwent obvious volume expansion during lithiation and shrinkage during delithiation. The TEM images in Fig. 1i–l

depict the lithiation-delithiation process in the 6th cycle (40–48 s). Similar volume changes were still observed, indicating stable, reversible performance of the yolk-shell NP.

Supplementary material related to this article can be found online at <http://dx.doi.org/10.1016/j.nanoen.2017.07.042>.

The inserted images in Fig. 1a–l show the volume changes of Sn core along with the applied voltages during reversible lithiation and delithiation cycling. The calculation method for volume measuring by Matlab program can be seen in the experimental section. From the inserted images in Fig. 1a–l, the volume change synchronizes with the applied rectangle voltage profile during cycling. Fig. 1m shows the volume expansion rate of the Sn core. The average volume expansion rate is more than 2, and even reaches to ~2.8 that can be calculated from the volume expansion curve in Fig. S2e. We observed that from the selected area electron diffraction (SAED) patterns that upon lithiation the Sn yolk changed to the $\text{Li}_{22}\text{Sn}_5$ phase (Fig. S2c), and after delithiation it returned back to the amorphous Sn phase (Fig. S2b). During the cycles, the Sn core were fully lithiated and delithiated, exhibiting the high reversibility and capacity retention.

2.2. Ultrafast reversible lithiation and delithiation cycling

We next characterize the lithiation and delithiation rate of the partially filled Sn@C yolk-shell NPs attached on the C substrate, as shown in Fig. 2 and Movie S2. The reversible lithiation-delithiation cycle time was further reduced to 2 s by controlling the signal function generator. The TEM images in Fig. 2a–j show the first two cycles of reversible lithiation and delithiation process. We observed that though a bias was applied at 0 s, lithiation was not started until 0.15 s, possibly due to the diffusion-limiting process. Despite of the delay, the Sn core was fully lithiated in the following 1 s (0.15–1.15 s) and then fully

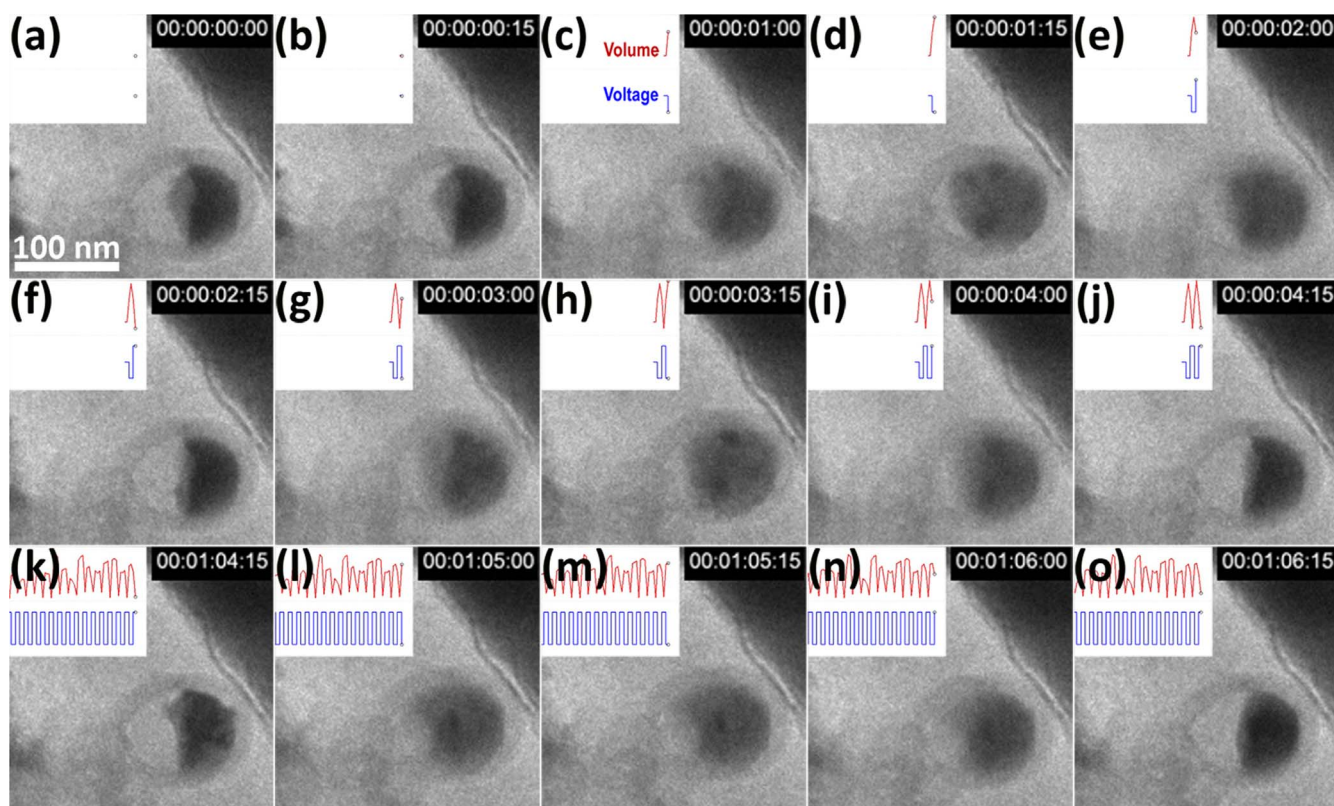


Fig. 2. *In situ* TEM ultrafast reversible lithiation and delithiation of another Sn@C yolk-shell NP attached on the C substrate. (a–j) TEM images of the first two cycles (0–4 s, the lithiation and delithiation time delayed for about 0.15 s, that is to say the NP had not been lithiated from 0 to 0.15 s or the lithiation started at 0.15 s, so we extended the image to 4.15 s) of reversible lithiation and delithiation process, the insert images show the volume changing of the target NP as the applied voltages in the reversible lithiation and delithiation processes. (k–o) TEM images of the 33th cycle (64.15–66.15 s) of reversible lithiation and delithiation process. The volume curve Vs. voltage curve also shows a perfect synchronization in the whole reversible lithiation and delithiation process. The lithiation and delithiation cycle time can be shortened to $t = 2$ s.

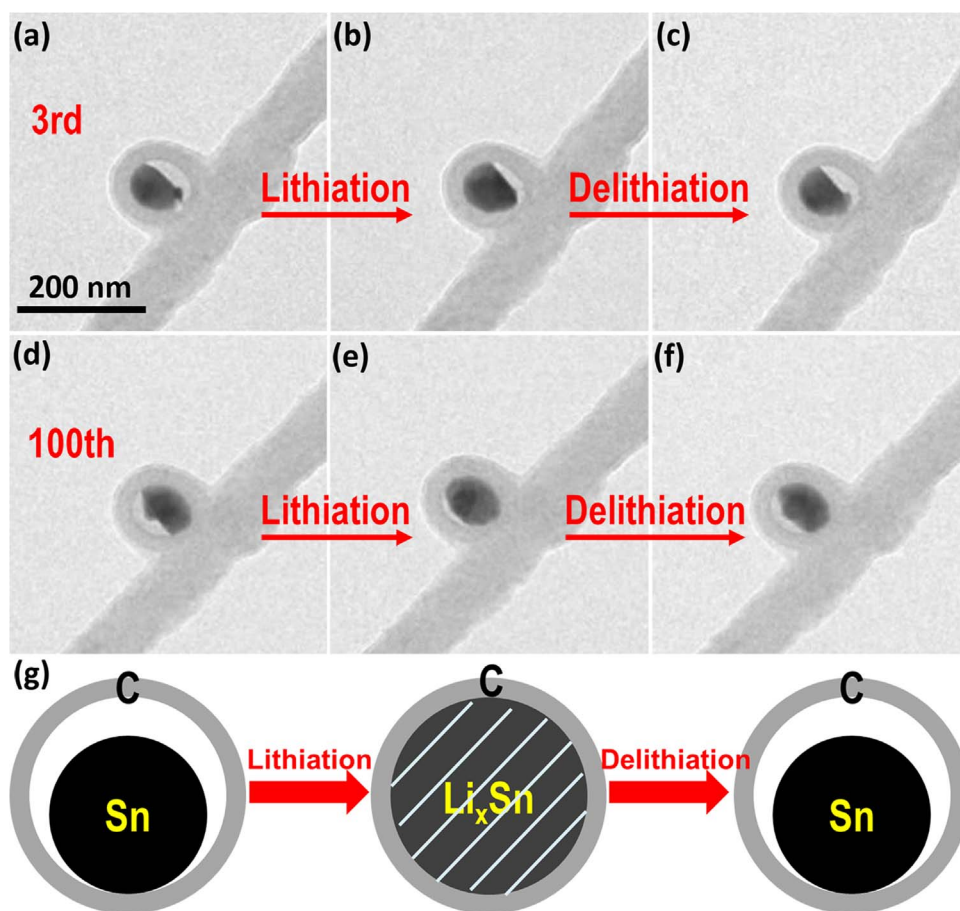


Fig. 3. *In situ* TEM cyclability of a Sn@C yolk-shell NP attached on the C fiber with $t=10$ s: (a–c) the third cycle, (d–f) the 100th cycle. (g) Schematic of the reversible lithiation and delithiation processes of the Sn@C yolk-shell NP.

delithiated within another 1 s (1.15–2.15), showing the ultrafast cycling rate. The inserted images show the NP volume changes consistently with the applied voltages during the reversible lithiation and delithiation processes. Such a synchrony between the volume change and applied bias remained in the 33th cycle (64.15–66.15 s), as shown in Fig. 2k–o. From the cycling time (2 s), the lithiation or delithiation rate was estimated to be > 100 nm/s. This compares to the lithiation

rate of ~ 27.5 nm/s of the C-coated SiNW [4], showing the ultrafast cycling of the Sn@C yolk-shell NPs. Similar ultrafast can be also realized for the Sn@C yolk-shell NPs attached onto C fibers, as shown in Fig. S3 and Movie S3.

Supplementary material related to this article can be found online at <http://dx.doi.org/10.1016/j.nanoen.2017.07.042>.

Besides the high energy capacity and ultrafast reversible

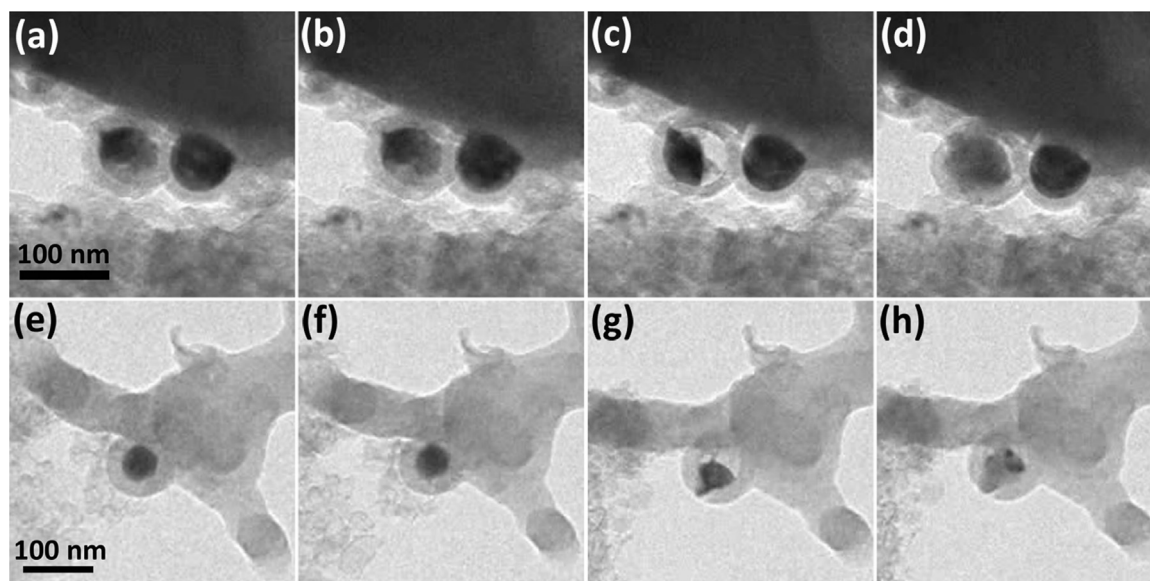


Fig. 4. The constraint effect of the coated C shell on the reversible lithiation and delithiation process of (a–d) the dispersed partially Sn@C core-shell NPs and (e–f) a nearly full NP attached on the C fiber. Comparing with the (a–b), (e–f) NPs with intact coated C shell, the volume changes of the NPs were more obvious when (c–d), (g–h) the coated C shell was broken.

performance, the Sn@C yolk-shell NPs can undergo hundreds of cycles with negligible degradation. Fig. 3 and Movie S4 show the multiple cycling performance of a Sn@C yolk-shell NP attached on the C fiber with each cycle duration of 10 s Fig. 3a-c shows the third cycle of the reversible reaction behavior of the sample, wherein the volume change upon lithiation and delithiation can be clearly seen. Fig. 3d-f shows structural changes of the NP in the 100th cycle, which shows negligible differences from those in the first several cycles. The yolk-shell structures in Figs. 1 and 2, S3 were well preserved after 130, 180, and 250 cycles, demonstrating its structural and electrochemical stability and durability.

Supplementary material related to this article can be found online at <http://dx.doi.org/10.1016/j.nanoen.2017.07.042>.

Then, the protective function of the C shell on the Sn core in the reversible lithiation and delithiation processes has also been probed. The loose C shell could successfully protect the Sn core from the rupture during the volume expansion in previous reports [11,16,17,19]. It is noteworthy that not all the Sn@C yolk-shell NPs keep intact in the reversible lithiation processes. So determinations of parameters like the ratio of the C shell thickness (t) to the Sn core diameter (d) t/d and the volume fraction ratio of Sn core in the C shell V_{Sn}/V_C (V_{Sn} : the volume of the Sn core, V_C : the volume wrapped by the C shell) are critical for effective protection of Sn core. Besides the protective function, the C shell also performs significant influence on the reversible reaction rate and the conductivity. The combined effects of the C shell on the Sn core can be defined as constraint effects. Considering the conductivity, the reversible reaction rate, and the protective function, the optimum t/d and V_{Sn}/V_C are distributed between 0.1–0.3 and 0.4–0.7, respectively. The details can be seen in the experimental section.

Fig. 4 shows the *in situ* TEM lithiation and delithiation behavior of two almost full Sn@C core-shell NPs attached on the C substrate and fiber before (Fig. 4a-b,e-f) and after rupture (Fig. 4c-d,g-h) with the same cycle time of 4 s. The videos are shown in Movies S5,6. From the images, it can be seen that the volume expansion and shrinkage of the Sn core in the reversible lithiation and delithiation after rupture (Fig. 4c-d,g-h, Sn leakage occurred) is more obvious than before (Fig. 4a-b,e-f), which is the volume constraint effect.

Supplementary material related to this article can be found online at <http://dx.doi.org/10.1016/j.nanoen.2017.07.042>.

2.3. Front track finite element modeling

In order to describe the transformation details in the lithiation process (the delithiation process is the opposite process of lithiation process, so it is omitted in the simulation), the front track finite element modeling is used to interpret the transformation steps. The video is shown in Movie S7. Fig. 5 shows the simulation results at different stages. Fig. 5a shows the initial state of the NP before lithiation. The first lithiation step starts in Fig. 5b with the negative voltage applied, and finishes in Fig. 5c with the fully transformation from Sn to Li_2Sn_5 [11]. It can be noticed that the volume expansion is limited in the first lithiation step. However, when the first lithiation step is finished, the second lithiation step starts as soon as possible as in Fig. 5d with obvious volume expansion. In Fig. 5e, the space is fully filled as the lithiation continuous. But the lithiation process keeps going until to the NP is fully lithiated accompanied with volume expansion of the whole NP that are shown in Fig. 5f-h. In this step, even though there are many types of intermediate products, the final product is demonstrated to be polycrystalline $Li_{22}Sn_5$ (Fig. S2c-d).

Supplementary material related to this article can be found online at <http://dx.doi.org/10.1016/j.nanoen.2017.07.042>.

In order to highlight the advantages of the partially filled Sn@C yolk-shell NP, the lithiation processes of pure Sn NP and full-filled Sn@C core-shell NP were also simulated by front track finite element modeling. The video is shown in Movie S8. Fig. S4 shows the simulation results of the pure Sn NP (left side in each image) and the full-filled Sn@C core-shell NP (right side in each image) at different stages. Fig. 5a shows the initial states of the two type NPs before lithiation. The first lithiation step of the two type NPs starts in Fig. S4b with the negative voltage applied. To the pure Sn NP, the first lithiation step finishes with fully transformation from Sn to Li_2Sn_5 in Fig. S4c left, and then the second lithiation step starts and finishes in Fig. S4d left and Fig. S4e left, respectively. To the Sn@C core-shell NP, the first lithiation step keeps going on in Fig. S4c-e right until to the moment in Fig. S4f right; then the second lithiation step starts in Fig. S4g right, and finishes in Fig. S4h right. The volume expansion of both the two type NPs in the first lithiation step is not so obvious compared with the second lithiation step.

Supplementary material related to this article can be found online at <http://dx.doi.org/10.1016/j.nanoen.2017.07.042>.

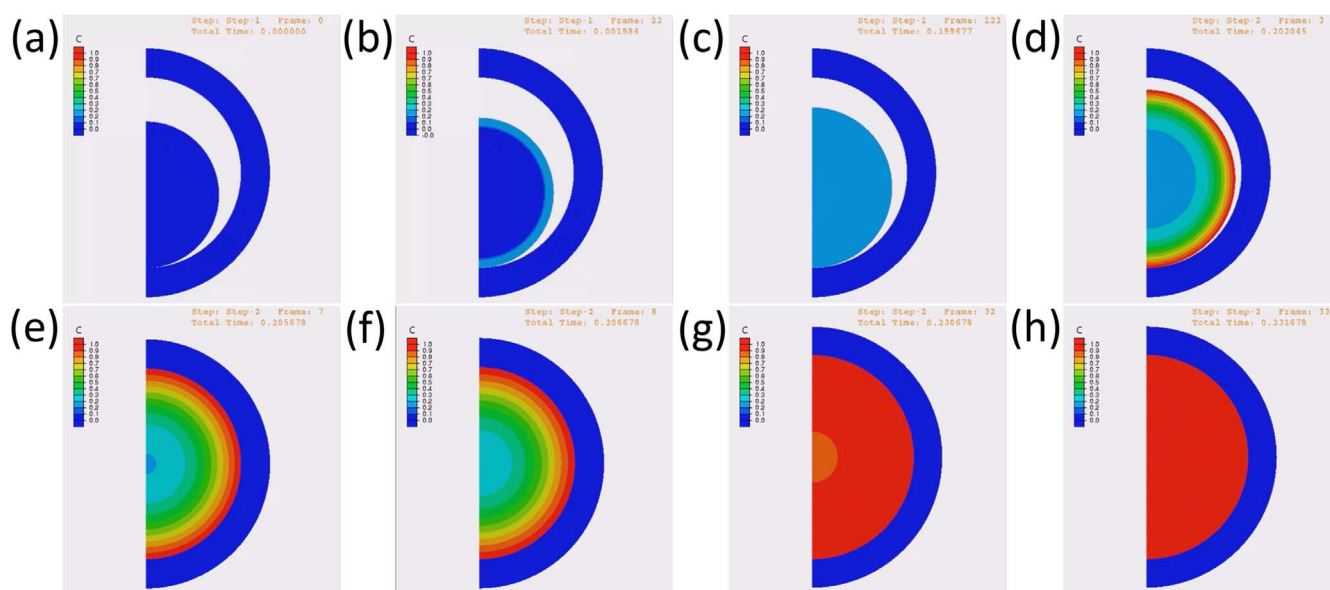


Fig. 5. Front tracking finite element analysis of the lithiation process of the Sn@C yolk-shell NP: (a) before lithiation, (b) the first lithiation step starts, (c) the first lithiation step is finished, (d) the second lithiation step starts, (e) the void in partially filled NP is filled full, (f-h) lithiation keeps going until to the NP is fully lithiated accompanied with volume expansion of the whole NP.

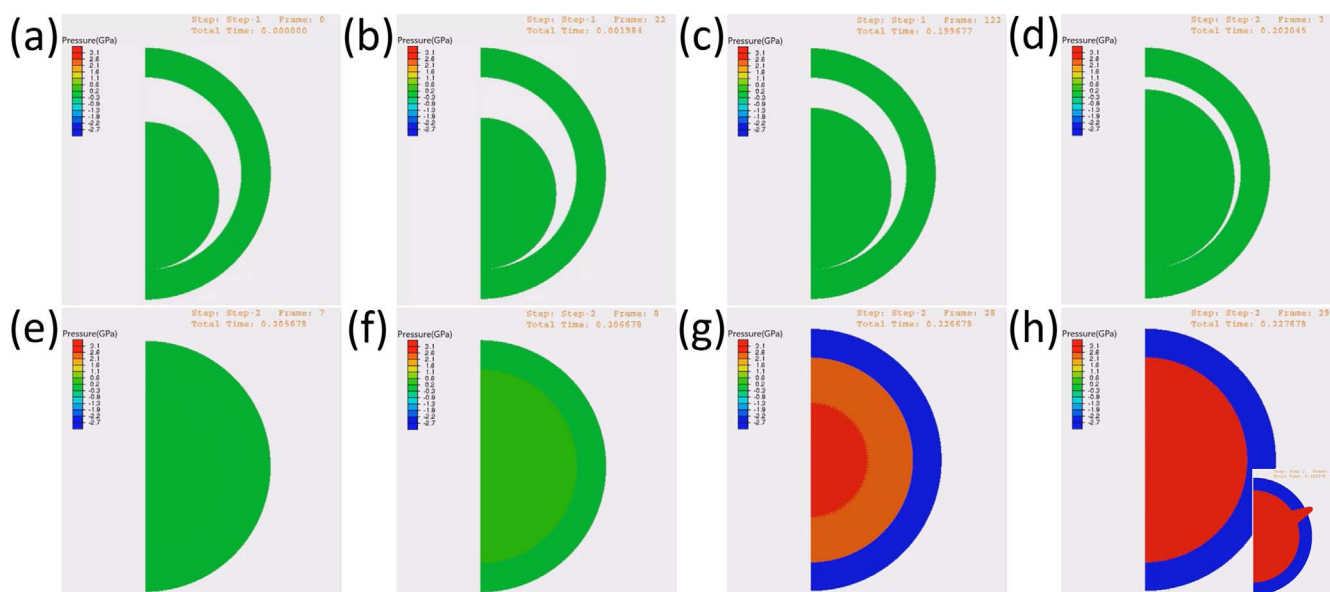


Fig. 6. Front tracking finite element analysis of pressure in the lithiation process of the Sn@C yolk-shell NP: (a) before lithiation, (b) the first lithiation step starts, (c) the first lithiation step is finished, (d) the second lithiation step starts, (e) the void in partially filled NP is filled full, from (a) to (e), there exists no pressure in the NP because of the freely void in the NP, (f–h) the NP is lithiated continually till to fully lithiated accompanied with volume expansion of the whole NP and the pressure coming from the extrusion between the inner Li_xSn_y and the outer C shell, and the extrusion in the inner Li_xSn_y itself. If the pressure reached to the critical fracture strength of the C shell while the lithiation has not finished yet, the C shell would fracture in the continuous lithiation process like the inset image in (h).

The pressure changes of the partially filled Sn@C yolk-shell NP in the lithiation process (the delithiation process is the opposite process of lithiation process, so it is omitted in the simulation) are simulated by front track finite element modeling. The video is shown in Movie S9. Fig. 6 exhibits the simulation results at different stages. Fig. 6a shows the initial state of the NP before lithiation. The first lithiation step starts in Fig. 6b with negative applied voltage and ends in Fig. 6c with the entire transformation of Sn to Li_2Sn_5 [11]. The second lithiation step starts as soon as the first lithiation step ends as depicted in Fig. 6d. In Fig. 6e, the space is fully filled with the lithiation continuous, so there is no pressure in the NP before it getting full because of the freely space in the NP. In Fig. 6f–h, the NP is continually lithiated accompanied with volume expansion of the whole NP and pressures that from the extrusion between the inner Li_xSn_y and the outer C shell, and the extrusion in the inner Li_xSn_y itself. If the inner pressure reached the critical fracture strength of the C shell while the lithiation has not finished yet, the C shell would fracture in the continuous lithiation process as shown in the inset image of Figs. 6h and 4c–d, g–h. The volume expansion is not so obvious in the second lithiation step after full-filling the void as before, which reveals the obvious constraint effect of the C shell on the volume expansion during the lithiation process.

Supplementary material related to this article can be found online at <http://dx.doi.org/10.1016/j.nanoen.2017.07.042>.

In addition, pressure changes of pure Sn NP and full-filled Sn@C core-shell NP in the lithiation processes are also simulated by front track finite element modeling. The video is shown in Movie S10. Fig. S5 exhibits the simulation results of the Sn NP (left in each image, no obvious pressure because of in free volume expansion state, and so no illustration about the pure Sn NP in the following texts) and the full-filled Sn@C core-shell NP (right in each image) at different stages. Fig. S5a shows the initial states of the two type NPs before lithiation. The first lithiation step of the two type NPs starts in Fig. S5b with the negative applied voltage, and the pressure (from the extrusion between the inner Li_xSn_y and the outer C coating, and the extrusion in the inner Li_xSn_y itself) appears in the Sn@C core-shell NP. To the pure Sn NP, the first lithiation step of the Sn NP ends with the entire transformation from Sn to Li_2Sn_5 [11] in Fig. S5c left, and then the second lithiation step of the Sn NP starts and ends in Fig. S5d left and Fig. S5e left,

respectively. To the Sn@C core-shell NP, the first lithiation step keeps going on and the pressure increases slowly from Fig. S5c right till to the moment in Fig. S5f right; the second lithiation step starts and the pressure increases rapidly from the moment in Fig. S5g right, and ends in Fig. S5h right with the maximum pressure. If the pressure reached the critical fracture strength of the C coating, the C shell would fracture in the continuous lithiation process as shown in the inset image in Fig. S5h right and Fig. 5c–d, g–h. It is obviously that the Sn core without C shell ends the lithiation process earlier compared with the Sn core coated with C shell. So the C shell has also introduced the constraint effect on the reversible lithiation and delithiation rate. It is different from the result that the C shell improves the rate parameters of Si NWs from 2.3 nm/s to 27.5 nm/s [4].

Supplementary material related to this article can be found online at <http://dx.doi.org/10.1016/j.nanoen.2017.07.042>.

3. Conclusions

In summary, the partially filled Sn@C yolk-shell NPs were designed and synthesized by CVD as anode materials for LIBs. The yolk-shell NPs can lithiate and delithiate hundreds of cycles with ultrafast (2 s per cycle) reversible cycling without rupture that was demonstrated by *in situ* TEM investigation. Compared to the naked SnNPs and fully filled Sn@C core-shell NPs, the chemomechanical durability of the yolk-shell NPs was improved through the coupled chemical reaction, diffusion, and stress generation upon lithiation that was proved by front tracking finite element analysis. The constraint effects of C coating on Sn core was also observed by TEM and illustrated by front-tracking finite element analysis. The results provide rational guidance to the development and optimization of yolk-shell NPs as high-performance anode materials for LIBs.

4. Experimental section

The partially filled Sn@C yolk-shell NPs used in our research were synthesized by CVD. Firstly, the SnO_2 (0.01 g) powder was ultrasonicated in an ethanol solvent (40 ml) for 2–4 h, dropped on a dry strip of filter paper, and transferred to the oven (60 °C) for 6 h. Secondly, the

dry strip of filter paper with SnO₂ was sent to the tube furnace and kept at 750 °C and a flow of Ar (200 sccm) and C₂H₂ (35 sccm) for 60 min. Thirdly, the sample was kept at 1000 °C for 3 h to volatilize part of Sn wrapped in the C shell. Finally, the sample was obtained when the temperature was dropped to room temperature under the protection of Ar (200 sccm).

The typical TEM images and corresponding SAED pattern of the perfect Sn@C yolk-shell NPs are shown in Fig. S6a–c,e. From the images, it can be seen that the Sn core is wrapped in the C shell with a certain void. The diameter of the Sn core (or the inner diameter of the C shell) is about 90 ± 30 nm, and the thickness of the C shell is about 10–20 nm. Under different synthesis conditions, some Sn@C yolk-shell NPs with other morphologies were also obtained that are shown in Fig. S6d,f. The synthesis parameters of the Sn@C yolk-shell NPs in Fig. S6d–f are listed in Table S1. In addition, the ratio of the C shell thickness to the Sn core diameter t/d also needs to be considered. If the t/d ratio is too high, the conductivity, the lithiation and delithiation rate would decrease (Fig. S6d); and if the t/d ratio is too low, the protective function of the C shell would be greatly reduced (Fig. S6f). Considering the conductivity, the lithiation and delithiation rate, and the protective function, the optimum t/d ratio is distributed between about 0.1 and 0.3 (Fig. S6e).

The volume fraction ratio of Sn core in the C shell $V_{\text{Sn}}/V_{\text{C}}$ (V_{Sn} : the volume of the Sn core, V_{C} : the volume wrapped by the C shell) can be controlled by the synthesis technology. If the volume fraction ratio exceeds the upper limit, Sn@C yolk-shell NPs would rupture in the lithiation process that is shown in Fig. S7a–b. If the volume fraction ratio exceeds the lower limit, Sn@C yolk-shell NPs cannot fill fullness in the lithiation process that is shown in Fig. S7c–d. The optimum $V_{\text{Sn}}/V_{\text{C}}$ of Sn@C yolk-shell NPs is distributed between about 0.4–0.7 that can guarantee the lithiated Sn core fill the C shell fullness as far as possible, and avoid the rupture of the Sn@C yolk-shell structure simultaneously in the lithiation process (Fig. S7e–f). The samples in Figs. 1–3 and Fig. S3 can demonstrate the speculation. The volume can be observed accurately by tilting the TEM holder. Fig. S8 show the TEM images of a Sn@C yolk-shell NPs at different tilt angles. Under the optimum tilt angle, the volume of the Sn NP is the smallest, and the image is uniform without contract difference.

In this letter, the reversible lithiation and delithiation behavior of the Sn@C yolk-shell NPs was investigated by means of *in situ* TEM. The Sn@C yolk-shell NPs were attached on the C substrate or the fiber that were stuck on the Au electrode by the conducting epoxy. The Li source was stuck on the Ni/Cr counterelectrode by the conducting epoxy. The Ni/Cr counterelectrode can move in the X, Y, Z directions driven by the piezoelectric ceramic tube. When the Sn@C yolk-shell NPs attached on the C substrate or the C fiber contacted the Li source, a cyclical rectangular wave voltage [−4 V, 4 V] was applied on the half-cell LIB by a function generator (Tektronix TBS1102) to observe its reversible lithiation and delithiation behavior.

The volume changes of the Sn core in the reversible reaction can be approximately calculated by the Matlab program. The video is shown in Movie S11. Firstly, the target video about the Sn@C yolk-shell NP (the sample was taken from Fig. 2) is cut down from the whole video. Then, the pixels A (the area of the pixels) of the Sn core in the target video is captured by Matlab program through the volume changes. Finally, the volume changing curve V ($V = \frac{4}{3}\pi^{-1/2}A^{3/2}$) can be exported by the transformation of the Matlab program. The TEM images, the pixels A images, and the volume changing curve are shown in the top left, top right, and bottom of Fig. S9a–h, respectively (1–4.5 s).

Supplementary material related to this article can be found online at <http://dx.doi.org/10.1016/j.nanoen.2017.07.042>.

The electrochemical performances of the macro battery were also measured. The above image in Fig. S10a shows the electrochemical performances of Sn@C yolk-shell NPs electrode cycled between 0.01 and 3.0 V at current densities of 500 and 1000 mA/g. The reversible discharge specific capacity is about 294 mAh/g at current density of

500 mA/g, and 262 mAh/g at current density of 1000 mA/g after 100 cycles. This low specific capacity is because the low weight percentage of Sn in the sample (Sn@C NPs and carbon substrate or fiber). As described in the experiment section, only two or three pipette drop of SnO₂ solution was dropped on a dry strip of filter paper (about 1 × 4 cm²) for the convenience of *in-situ* TEM investigation of Sn@C yolk-shell NPs, thus the weight percentage of Sn in the final sample is very low. If the proportion of carbon substrate or fiber decreased, the capacity of the sample would be increased greatly. This image demonstrates a remarkable cycling stability over 100 cycles for Sn@C yolk-shell NP electrode at the current density of 500 and 1000 mA/g, after 100 cycles, the electrode can still reach the specific capacity of 294 and 262 mAh/g. The inset image in Fig. S10a reveals the discharge capacity of Sn@C yolk-shell NP electrode at different current density (200, 500, 1000, 2000, 4000, 200 mA/g). The rate performance of the Sn@C powders is shown in this figure, in which the current densities increased stepwise from 200 mA/g to 4000 mA/g and then returned to 200 mA/g. The cycles were measured during each increment to evaluate the rate performances. The 10th reversible discharge capacities of the Sn@C powders decreased from 261 mAh/g to 184 mAh/g as the current density increased from 200 to 4000 mA/g. Despite cycling at high current densities, the discharge capacity of the powders recovered to 291 mAh/g when the current density returned to 200 mA/g. The image in Fig. S10b shows the cycle voltammograms of Sn@C yolk-shell NPs with scan speed of 0.2 mV/s. The peak below 0.25 V (0.156 V and nearly 0.01 V) corresponds to the Sn alloy reaction to form Li_xSn, and the intercalation of Li⁺ into carbon shell results in forming of Li_xC. The peak at 0.643 V in the first cycle is probably attributed to form a SEI layer. In the first anodic scan, the peak at 0.165 V corresponds to the dealloying of Li_xSn.

Notes

The authors declare no competing financial interest.

Acknowledgments

This work is financially supported by the National Natural Science Foundation of China (No.11672355).

Appendix A. Supporting information

Supplementary data associated with this article can be found in the online version at <http://dx.doi.org/10.1016/j.nanoen.2017.07.042>.

References

- [1] E.J. Yoo, J. Kim, E. Hosono, H.S. Zhou, T. Kudo, I. Honma, *Nano Lett.* 8 (2008) 2277–2282.
- [2] M.G. Kim, J. Cho, *Adv. Funct. Mater.* 19 (2009) 1497–1514.
- [3] M.G. Kim, S. Lee, J.J. Cho, *Electrochem. Soc.* 156 (2009) A89–A94.
- [4] X.H. Liu, L.Q. Zhang, L. Zhong, Y. Liu, H. Zheng, J.W. Wang, J.H. Cho, S.A. Dayeh, T. Picraux, J.P. Sullivan, S.X. Mao, Z.Z. Ye, J.Y. Huang, *Nano Lett.* 11 (2011) 2251–2258.
- [5] R. Yazami, P.J. Touzain, *J. Power Sources* 9 (1983) 365–371.
- [6] W.J. Zhang, *J. Power Sources* 196 (2011) 13–24.
- [7] C.K. Chan, H. Peng, G. Liu, K. McIlwrath, X.F. Zhang, R.A. Huggins, Y. Cui, *Nat. Nanotechnol.* 3 (2007) 31–35.
- [8] X.H. Liu, J.W. Wang, S. Huang, F.F. Fan, X. Huang, Y. Liu, S. Krylyuk, J. Yoo, S.A. Dayeh, A.V. Davydov, S.X. Mao, S.T. Picraux, S.L. Zhang, J. Li, T. Zhu, J.Y. Huang, *Nat. Nanotechnol.* 7 (2012) 749–756.
- [9] D. Larcher, S. Beattie, M. Morcrette, K. Edstroem, J.C. Jumas, J.M. Tarascon, *J. Mater. Chem.* 17 (2007) 3759–3772.
- [10] L. Beaulieu, J. Dahn, *J. Electrochem. Soc.* 147 (2000) 3237–3241.
- [11] Q.Q. Li, P. Wang, Q. Feng, M.M. Mao, J.B. Liu, S.X. Mao, H.T. Wang, *Chem. Mater.* 26 (2014) 4102–4108.
- [12] J.Y. Huang, L. Zhong, C.M. Wang, J.P. Sullivan, W. Xu, L.Q. Zhang, S.X. Mao, N.S. Hudak, X.H. Liu, A. Subramanian, H.Y. Fan, L. Qi, A. Kushima, J. Li, *Science* 330 (2010) 1515–1520.
- [13] Y.J. Zhu, J.W. Wang, Y. Liu, X.H. Liu, A. Kushima, Y.H. Liu, Y.H. Xu, S.X. Mao, J. Li, C.S. Wang, J.Y. Huang, *Adv. Mater.* 25 (2013) 5461–5466.

- [14] M.H. Kong, J.H. Noh, D.J. Byun, J.K. Lee, *J. Electroceram.* 23 (2009) 376–381.
 [15] M.H. Kong, D.J. Byun, J.K. Lee, *Adv. Mater. Process.* 26 (2007) 333–336.
 [16] L.Q. Zhang, X.H. Liu, Y. Liu, S. Huang, T. Zhu, L.J. Gui, S.X. Mao, Z.Z. Ye, C.M. Wang, J.P. Sullivan, J.Y. Huang, *ACS Nano* 5 (2011) 4800–4809.
 [17] L.L. Luo, P. Zhao, H. Yang, B. Liu, J.G. Zhang, Y. Cui, G.H. Yu, S.L. Zhang, C.M. Wang, *Nano Lett.* 15 (2015) 7016–7022.
 [18] T. Ishihara, M. Nakasu, M. Yoshio, H. Nishiguchi, Y. Takita, *J. Power Sources* 146 (2005) 161–165.
 [19] X.H. Liu, L. Zhong, S. Huang, S.X. Mao, T. Zhu, J.Y. Huang, *ACS Nano* 6 (2012) 1522–1531.



Ke CAO is currently a doctor candidate in City University of Hong Kong. He received his master's degree in School of Materials Science & Engineering at Zhejiang University (2016), China. His research interests focus on *in situ* transmission electron microscopy (TEM) characterization of mechanical and electromechanical behavior of low-dimensional nanomaterials.



Peifeng Li is currently a postdoctoral in Zhejiang University. He received his Ph.D. degree in University of Science and Technology Beijing (2015), M.S. degree in Northeastern University (2010), and B.S. degree in Shandong University of Science and Technology (2008). His current research interests focus on *in situ* transmission electron microscopy (TEM) and scanning electron microscopy (SEM) for investigating the properties and service behaviors of nanomaterials under mechanical and electrical fields.



Yizhi Zhang is currently a doctor candidate in Zhejiang University. He received his B.S. degree in Zhejiang University (2015). His current research interests focus on developing equipments for *in situ* transmission electron microscopy (TEM) experiments of material science.



Tianwu Chen received his B.S. degree in engineering mechanics from Dalian University of Technology (2012) and M.S. degree in solid mechanics from Peking University (2015). He is currently pursuing his doctoral degree in The Pennsylvania State University. His current research focuses on the mechanics of high-capacity anode/cathode materials in lithium/sodium-ion batteries and mechanical energy harvesters.



Xu Wang received her Bachelor's degree in Minnan Normal University in 2011. Now, she is a Ph.D. candidate at Department of Physics of Zhejiang University. Her research focus on nanostructure based composite materials and their application in lithium ion batteries.



Sulin Zhang is a Professor of Engineering Science & Mechanics, and Biomedical Engineering at The Pennsylvania State University. His group performs computational and experimental research on mechanics of materials, mechanics of energy storage and conversion, and mechanobiology. He received a PhD in from UIUC in 2002, MS from Tsinghua University in 1997, and BS from Dalian University of Technology in 1994, all in Applied Mechanics. He is a recipient of the 2007 National Science Foundation Career Development Award.



Jiabin Liu is currently an associate professor in Zhejiang University (ZJU). He received his Ph.D. degree and B.S. degree in Zhejiang University at 2009 and 2004. His current research interests focus on *in situ* TEM for investigating the properties and service behaviors of nanomaterials/metals under mechanical fields.



Hongtao Wang is a professor of Applied Mechanics of Zhejiang University, China. He received his B.S. degree and Ph.D. degree in Tsinghua University at 2000 and 2004, and another Ph.D degree in Harvard University in 2009. He has been awarded the financial support for outstanding young scientist foundation of China in 2017. His research focuses on micro-nano mechanics and new energy materials by *in situ* TEM technique.